3. Oceanic response to the atmospheric forcing.

1. Sea surface temperature

The mechanisms of sea surface temperature changes are different in the equatorial regions and in the mid latitudes. Let us consider the main balance of terms in the sea surface temperature equation. If $\vartheta(x,t)$ denotes temperature, the temperature equation can be written

$$\vartheta_t + u\vartheta_x + v\vartheta_y + w\vartheta_z = \frac{1}{\rho_0 C_p} q_{sw} + (\kappa \vartheta_z)_z + k(\vartheta_{xx} + \vartheta_{yy}) \tag{56}$$

where $q_{sw}(z)$ is the penetrating flux of short wave solar radiation, κ the vertical diffusivity, ρ the density, C_p the heat capacity of water, and the horizontal eddy diffusivity k is taken to be constant. If the variations of the free surface are neglected and the temperature and the velocity are assumed to be constant in the mixed layer, integration from the surface to just below the mixed layer at $z = -h$ yields the slab mixed-layer model

$$hT_t + h\,u\,T_x + h\,v\,T_y + H(w_e)(T - T_e)\,w_e = (Q(0) - Q(-h))\,/\,\rho\,C_p + \kappa\,h\,(T_{xx} + T_{yy}) \tag{57}$$

where the entrainment (or detrainment) velocity w_e is the rate at which fluid particules move vertically at the mixed layer bottom relative to the mixed layer bottom. It is given by

$$w_e = h_t + (hu)_x + (hv)_y$$

It is thus equal to zero if there are no mass exchanges between the mixed layer and the startified fluid below. The heaviside function $H(w_e)$, equal to 1 when $w_e > 0$ and the mixed layer deepens (entrainment), and zero otherwise (detrainment for a shallowing mixed layer), has been introduced in (57) since leaving fluid behind the mixed layer water (because mixing is not strong enough to reach the bottom of the mixed layer) does not change its temperature. $Q(0) = Q_s + Q_L + Q_{LW} + q_{sw}(0)$ is the surface heat flux, where Q_s is the sensible heat flux, Q_L the latent heat flux and Q_{LW} the longwave radiation, $Q(-h)$ is the heat flux at the mixed-layer base, and T_e the temperature of entrained water. Except when the mixed-layer is very shallow as in the eastern tropical Pacific (but the concept of a well mixed layer does not really apply), most of the solar radiation is absorbed in the mixed layer so that $Q(-h)$ mostly represents vertical mixing at the mixed layer base. In slab mixed-layer models, the mixed-layer depth h is determined by the turbulent kinetic energy budget. A simplified form of the vertically integrated energy budget is

$$\frac{1}{2}H(w_e)w_e\left[\alpha gh(T - T^-) - m_s\left|\mathbf{v} - \mathbf{v}^-\right|^2\right] = m_0 u_*^3 + \frac{1}{2}\frac{\alpha ghQ}{\rho C_p} - \varepsilon h$$

where u_* is the friction velocity related to the surface wind stress by $|\tau| = \rho \, u_*^2$, α is the coefficient of thermal expansion, ε the turbulent dissipation, and m_s and m_s are constant. The first term is the rate of working needed to lift and mix the denser entrained water, the second term is the rate of mean flow energy reduction by mixing across the mixed-layer base, the third term the wind generation of turbulent energy, the fourth one the rate of potential energy change produced by the surface heat flux, and the fifth term represent turbulent dissipation.

In the mid latitudes, the sea surface temperature is primarily determined by local air-sea interactions, except in the vicinity of fronts. The main balance is

$$hT_t + (T - T_e) \, w_e = Q(0), \tag{58}$$

so that the rate of change of the surface layer heat content is mostly controlled by the air-sea heat exchanges and the wind-driven entrainment flux. At the equator, however, all the terms in Eq. (56) are important. Both the zonal and the meridional advection play a role, and vertical mixing remains large in the stratified waters below the surface layer. Also, horizontal mixing can be large and complex, in particular in the presence of instability waves. As the surface currents and the vertical motions (which influence T_e) are in part remotely forced, the sea surface temperature is only partly controlled by the local air-sea interactions, and it also depend on the basin-wide wind stress forcing. This explains the decreasing value of the correlation between the local rate of change of sea surface temperature and the surface heat flux that is observed as one approaches the equator (Fig.18). In the tropics, the interactions between the ocean and the atmosphere cannot be studied without taking into account the ocean dynamics, and it is thus a more challenging task.
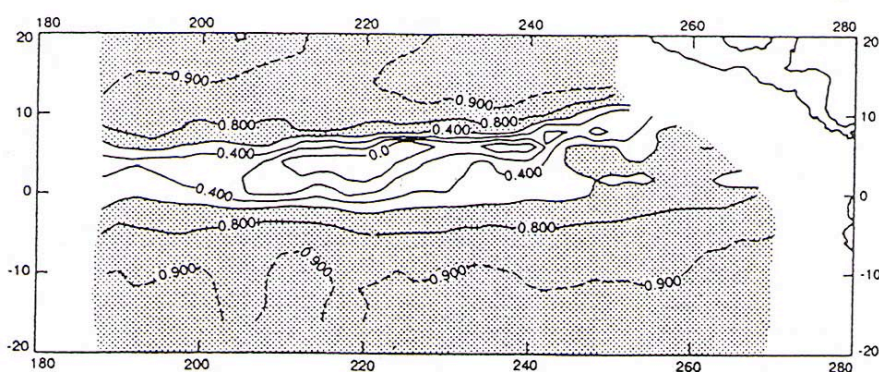

Fig. 18. Distribution of correlation coefficients between surface net heat flux and time rate of change of sea surface temperature during a 46-month period. (From Liu and Gauthier 1990).

The observations show that zonal, meridional and vertical temperature advection plays a large role in the SST anomaly changes in the equatorial Pacific, depending on season, location and SST conditions (Fig. 1.10 from Philander 1990). For instance, some Kelvin wave pulses
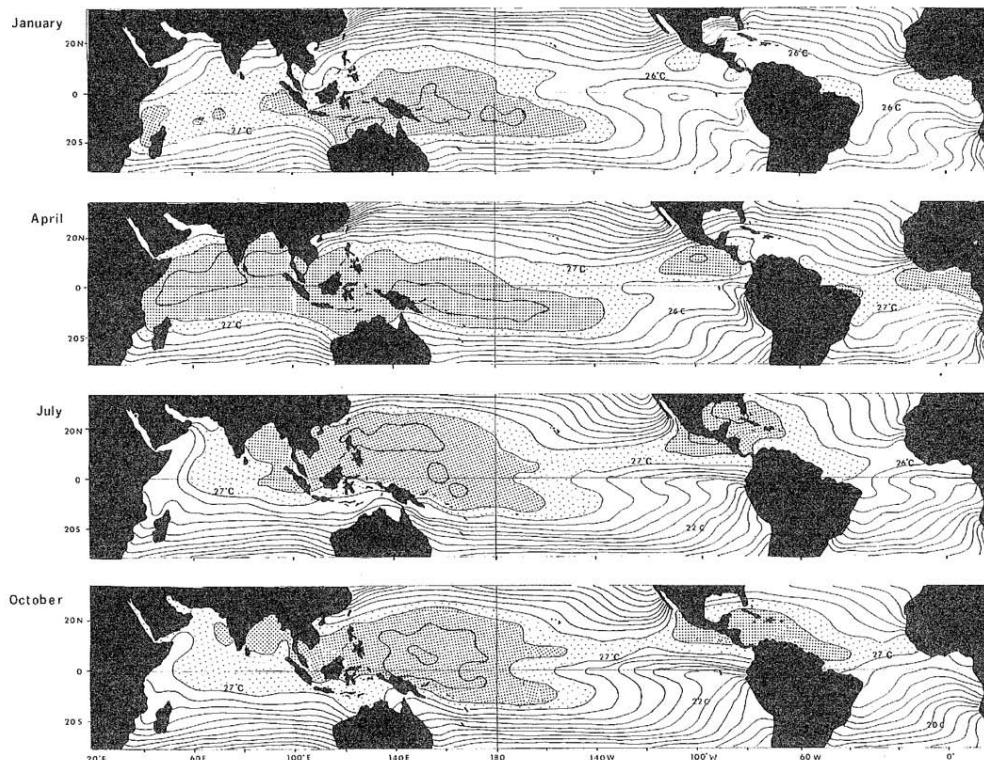
Figure 1.10. Climatological sea surface temperatures for January, April, July, and October. Regions with temperatures in excess of 27°C and 28°C are shaded. Averaging of the data causes a sharp thermal front near 3°N in the eastern Pacific and Atlantic in July and October to be diffuse. A wedge of cold surface waters off northeastern Africa in July is absent for similar reasons. (The data were provided by R. Reynolds of the Climate Analysis Center, NOAA, Washington, D.C.)

create large sea surface temperature changes, while others only have a small sea surface temperature signature. As discussed by Harrison and Schopf (1984), the differences are associated in part with the timing of the westerly wind bursts. The Kelvin wave primarily affects the sea surface temperature via zonal advection in the central ocean, whereas vertical advection and the alongshore currents associated with the coastally trapped reflected waves play the dominant role near the eastern coast. When the mean zonal sea surface temperature gradient is large along the equator as in summer and fall, the eastward advection associated with a downwelling Kelvin wave creates a positive sea surface temperature anomaliy in the central Pacific. Such process has been associated with the initiation of some El Niño events, as in 1982. On the other hand, when the mean zonal sea surface temperature gradient is weak as in winter and spring, zonal advection has a small effect and little sea surface temperature change is expected as the wave crosses the ocean (See Fig. 4 and 6). In the eastern Pacific, however, the shallow thermocline is deepened by the Kelvin wave (Fig.38) during a El Niño event, which shuts off the sea surface temperature cooling by upwelling since the latter is limited to the the upper part of the water column (Fig.9 de Halpern et al. 1988, les unités sont en 10^{-5} ms^{-1}).
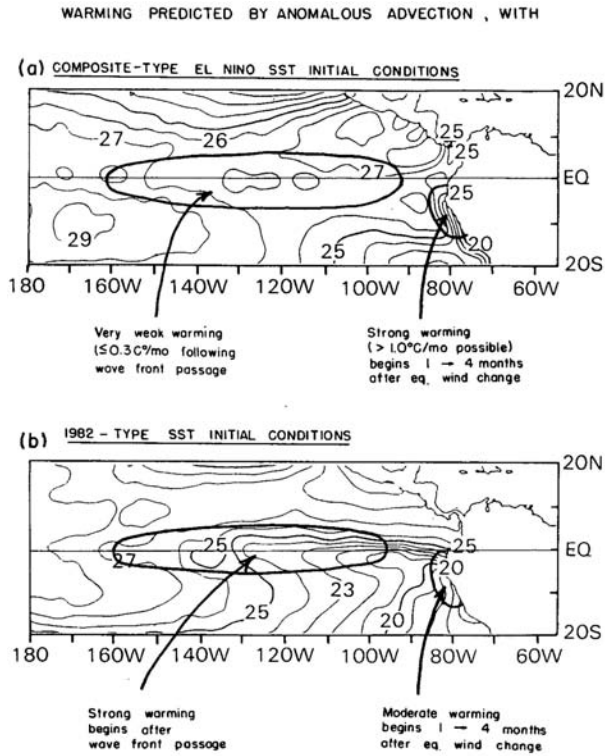
WARMING PREDICTED BY ANOMALOUS ADVECTION , WITH

(a) COMPOSITE-TYPE EL NINO SST INITIAL CONDITIONS

Very weak warming
(≤ 0.3C°/mo following
wave front passage

Strong warming
(> I.0°C/mo possible)
begins I → 4 months
after eq. wind change

(b) 1982-TYPE SST INITIAL CONDITIONS

Strong warming
begins after
wave front passage

Moderate warming
begins I → 4 months
after eq. wind change

FIG. 4. Schematic description of the timing and location of SST changes expected from the anomalous advection model. (a) The composite El Niño situation, with Kelvin wave front propagation near the beginning of the year; the first strong warming will occur at the coast. (b) The 1982 El Niño, with Kelvin wave front propagation near mid-year; the first observable warming will occur along the equator.

SIMULATED TEMPERATURE

SIMULATED ANOMALY

SIMULATED TEMPERATURE

SIMULATED ANOMALY
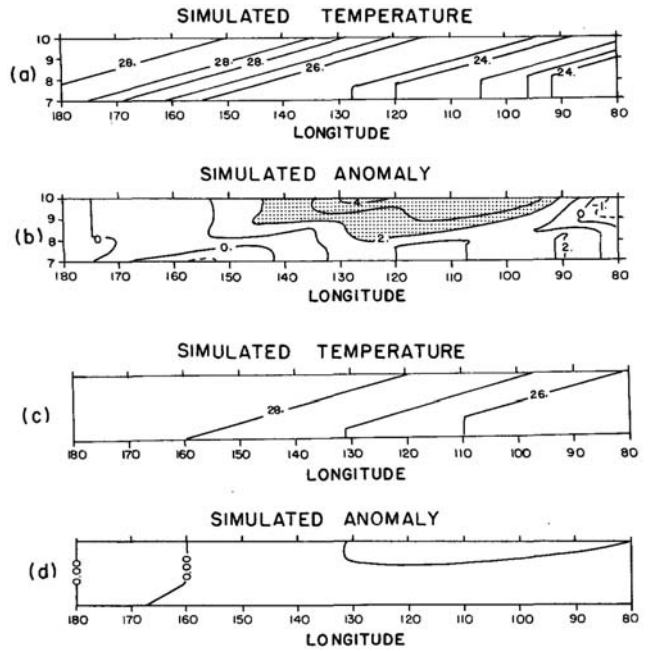
FIG. 6. Equatorial time–longitude behavior predicted by a simple anomalous advection model using 1982 conditions. (a) SST obtained with Kelvin wave passage in mid-year; July initial SST conditions. (b) SST anomaly from (a). (c) SST obtained with Kelvin wave passage in February–March; February initial SST conditions. (d) Change in SST from February. Wave frontal speed is taken to be 2.5 m s^{-1}; particle velocity behind the wave front is taken to be 0.60 m s^{-1}. See text for further explanation.

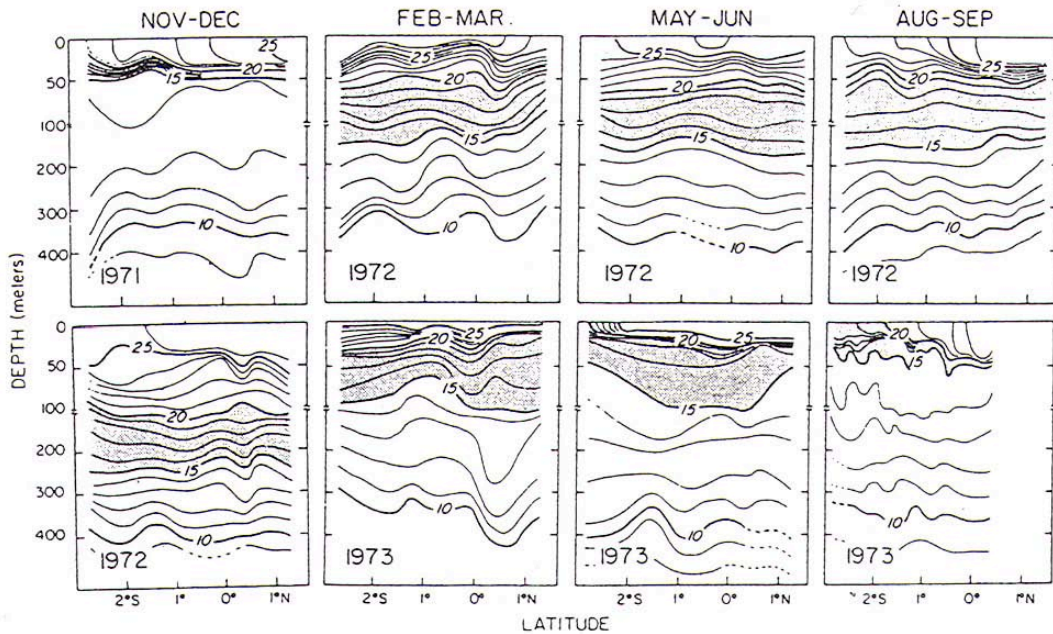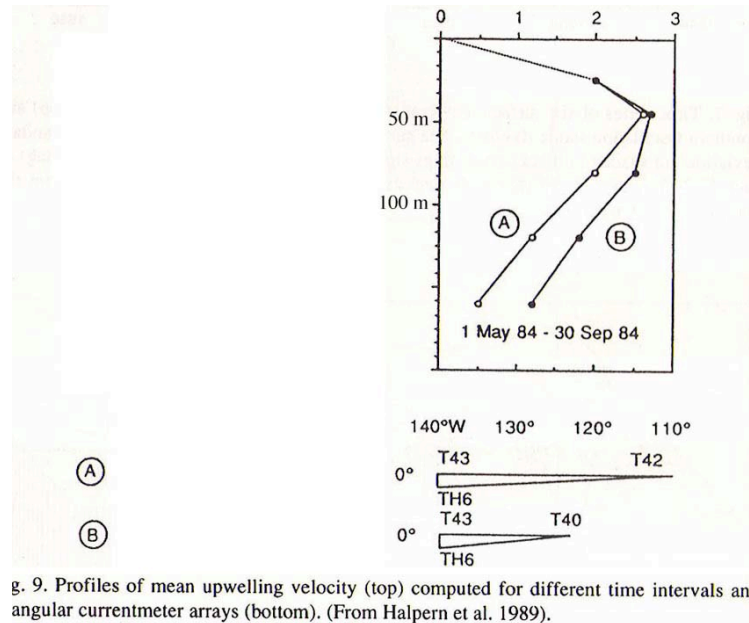Fig. 38. Eight successive ocean temperature (in °C) sections across the equator off Ecuador (82.5°W) at 3-month intervals before, during, and after the 1972-1973 El Niño. (From Enfield 1989).

g. 9. Profiles of mean upwelling velocity (top) computed for different time intervals and angular currentmeter arrays (bottom). (From Halpern et al. 1989).

In reality, both Kelvin and Rossby wave contribute to the SST anomaly advection, as illustrated for the 93-97 period by Boulanger and Menkes (1999). A quantitative estimation of the main terms in the SST anomaly equation has been done on long timescales by Wang and McPhaden (2001) and based on 4 TAO moorings along the equatorial Pacific, showing more explicitly the influence of upwelling or downwelling. They show that on intraseasonal timescales the SST variability is most affected by the surface heating in the western Pacific, zonal advection in the central Pacific, and vertical advection and entrainment in the eastern Pacific, with a strong influence of the Kelvin waves. Note that the surface heating always tends to damp the SST anomalies, so that it plays a passive role, not an active one as in the mid latitude.

The observations show that the SST anomalies are asymmetric in the tropical Pacific in the sense that the El Niño anomalies are not the opposite of the La Niña ones: the El Niño events tend to be larger than the La Niña events, and the spatial distribution is also different. This is an intrinsic nonlinear characteristic of the ENSO phenomenon. The nonlinearity clearly appears in the heat budget of the oceanic surface layer. Consider the temperature équation

$$\theta_t + u\theta_x + v\theta_y + w\theta_z = R \tag{59}$$

where R is the residual including heating, diffusion, etc. Let $T = \bar{T} + T'$. Replacing in (59) yields

$$\theta'_t + u'\bar{\theta}_x + v'\bar{\theta}_y + w'\bar{\theta}_z + \bar{u}\theta'_x + \bar{v}\theta'_y + \bar{w}\theta'_z = -(u'\theta'_x + v'\theta'_y + w'\theta'_z) + R' \tag{60}$$

which shows the nonlinear terms (quadratic in the perturbation) act as an equivalent heating or cooling term. For simplicity, their average (which should be subtracted) has been neglected in (60). The nonlinear dynamical "heating" depends on the correlation between the velocity and the

temperature anomalies, and it can be estimated from observations or model data. Its contribution in the first 50 m was estimated by An and Jin (JCLI 2004) from the NCEP predictionsystem (oceanic model with data assimilation) and is illustrated for two El Niño and
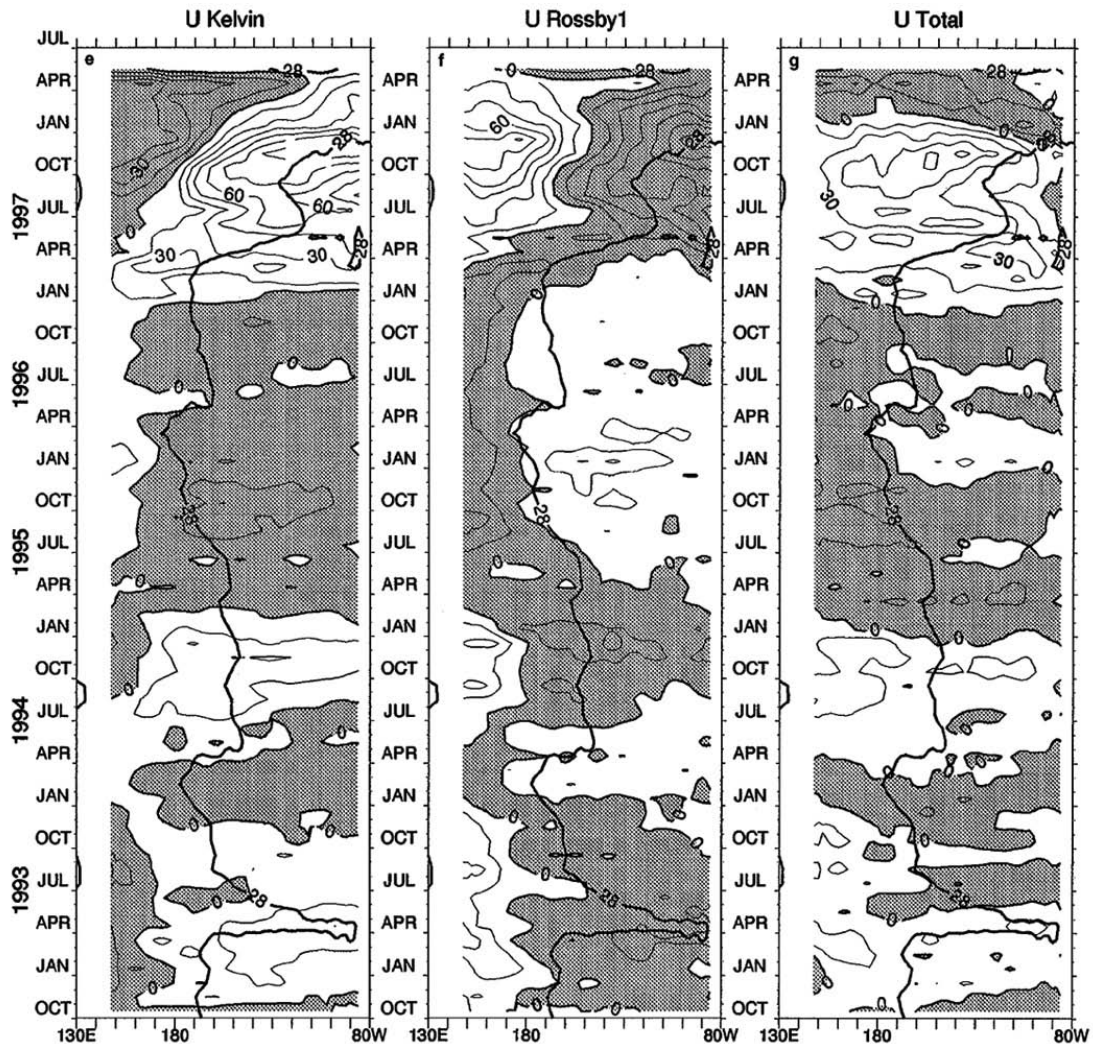

Fig. 11a–g From *left* to *right*, zonal sections of 2 °N–2 °S averaged: **a** monthly SST from the Climate Analysis Center (contours are every 1 °C); **b** monthly zonal wind stress interannual anomalies from ERS data (contours are in 10^{-2} N/m², every 2.10^{-2} N/m²); **c** monthly interannual SST anomalies from the Climate Analysis Center (contours are every 0.5 °C); **d** monthly interannual sea level anomalies from TOPEX/POSEIDON data (contours are every 5 cm); **e** contributions of Kelvin wave to interannual zonal current anomalies (contours are every 10 cm/s); **f** contributions of first-mode Rossby wave to interannual zonal current anomalies (contours are every 10 cm/s); **g** contributions of both the Kelvin and first-mode Rossby waves to interannual zonal current anomalies (contours are every 10 cm/s). All anomalies are computed relative to the 1993–1996 seasonal cycle. The 28 °C isotherm is superimposed onto each figure

two La Niña events (Fig.5). In all cases the nonlinear dynamical heating tends to warm the equatorial Pacific, thus reinforcing the El Niño SST anomalies but weakening the La Niña ones. The largest contribution comes from the vertical advective heating, with the zonal advective one second strongest. Note that the nonlinear dynamical heating is much stronger after 1980 than before, due to decadal changes in the stratification in the tropical Pacific, via $(T - T_e)$ in particular. This shows that nonlinearity strongly contributes to the phase asymmetry of the ENSO events.
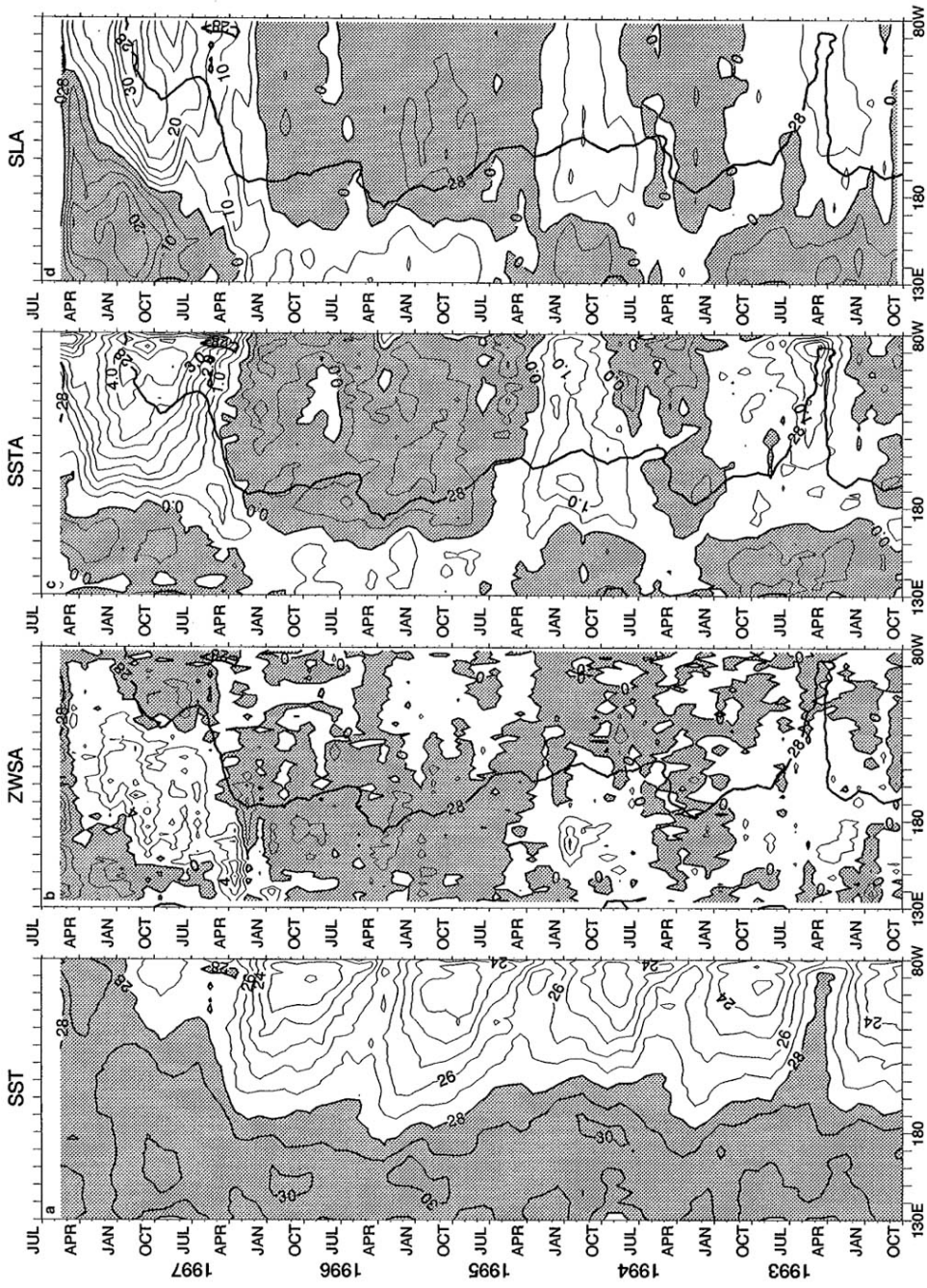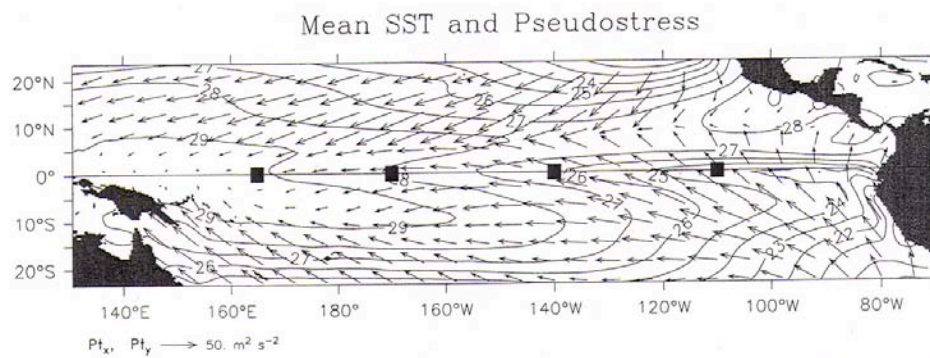
Fig. 11 (*Continued*)

Mean SST and Pseudostress

Pt_x, Pt_y ⟶ 50. m² s⁻²

FIG. 1. Mean SST (°C) based on the Reynolds and Smith (1994) analysis and mean pseudostress (m² s⁻²) based on FSU wind product in the tropical Pacific. Squares indicates locations of the TAO current mooring measurements used in this study.
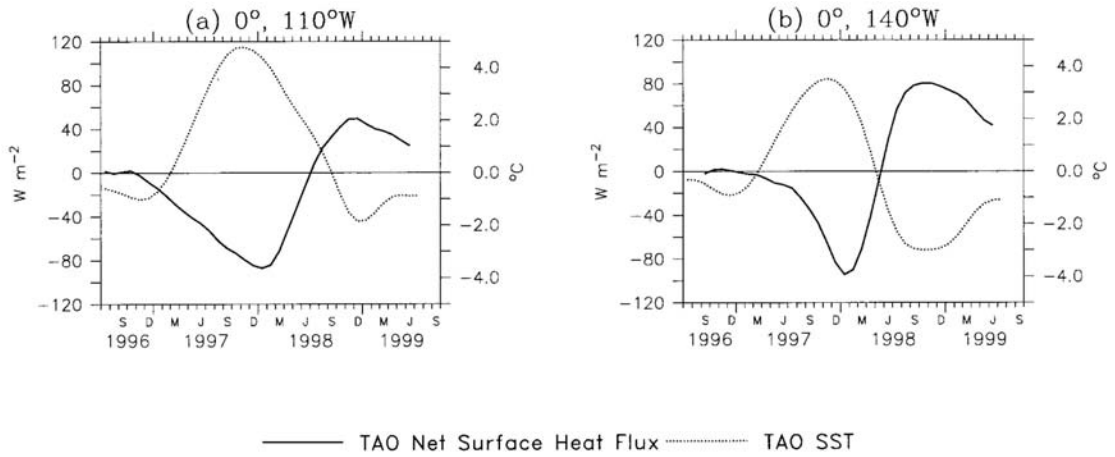
FIG. 5. Time series of interannual anomalies in net surface heat flux (solid line) and SST (dotted line) estimated from TAO data for the period of Jul 1996 to Sep 1999 on the equator at (a) 110°W, (b) 140°W, (c) 170°W, and (d) 165°E. Interannual anomalies were computed by subtracting out the mean seasonal cycle from individual monthly time series, then smoothing with a 5-month running-mean filter and a 3-month triangle filter.
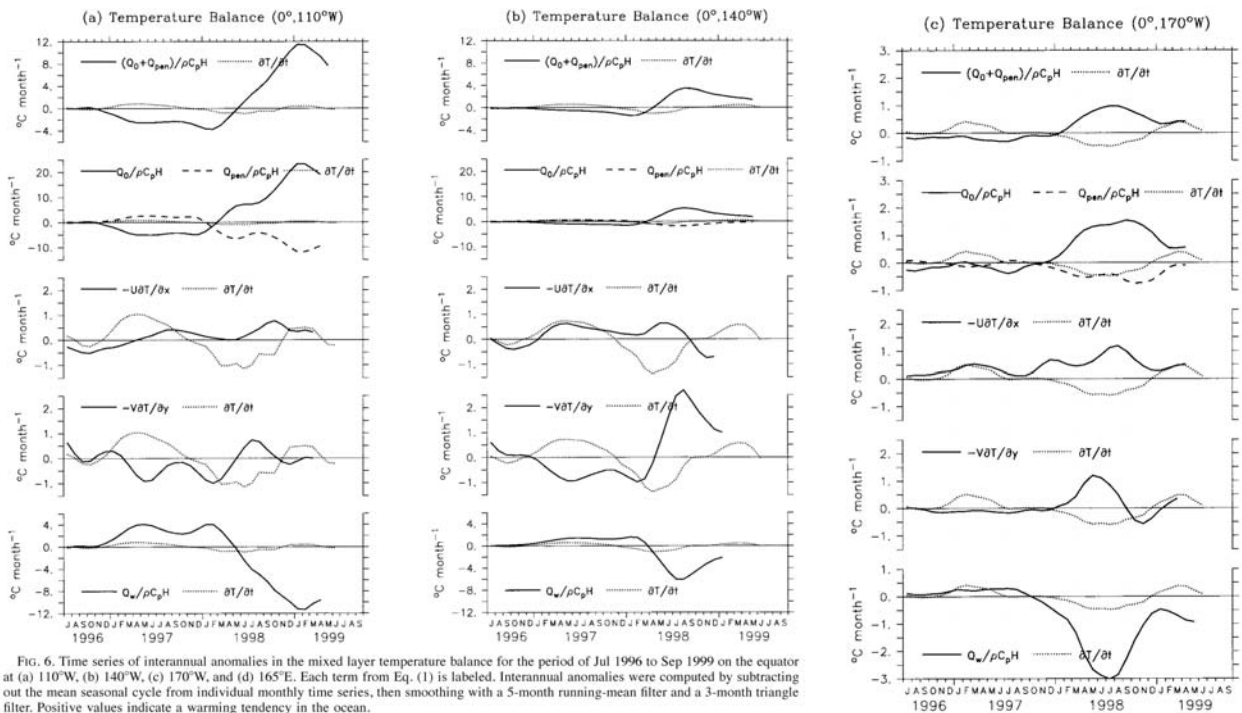

FIG. 6. Time series of interannual anomalies in the mixed layer temperature balance for the period of Jul 1996 to Sep 1999 on the equator at (a) 110°W, (b) 140°W, (c) 170°W, and (d) 165°E. Each term from Eq. (1) is labeled. Interannual anomalies were computed by subtracting out the mean seasonal cycle from individual monthly time series, then smoothing with a 5-month running-mean filter and a 3-month triangle filter. Positive values indicate a warming tendency in the ocean.
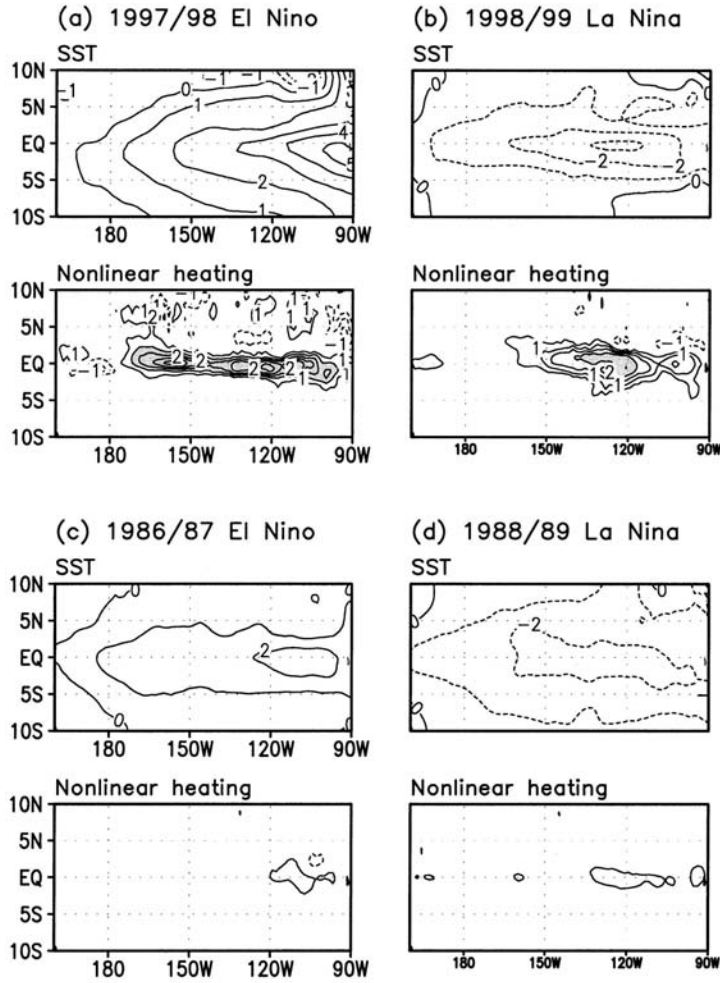
FIG. 5. SST anomaly (°C) and rate of change in SST (°C month⁻¹) due to the nonlinear dynamic heating during (a) the 1997/98 El Niño (Jul 1997–May 1998), (b) the 1998/99 La Niña (Jul 1998–May 1999), (c) the 1986/87 El Niño (Oct 1986–Aug 1987), and (d) the 1988/89 La Niña (Jul 1988–May 1989).
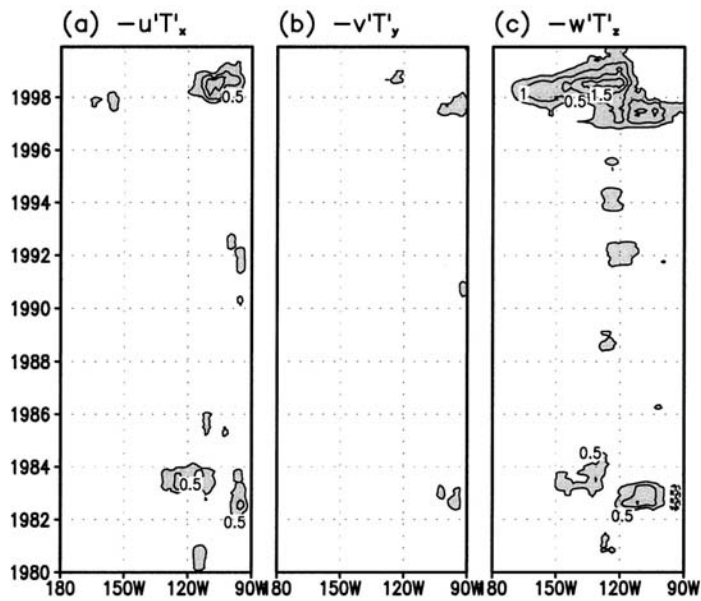

FIG. 7. Time–longitude cross section of the nonlinear dynamic heating rate (°C month⁻¹) due to (a) zonal advection, (b) meridional advection, and (c) vertical advection along the equator (1°N–1°S). The 11-month running mean has been used.

2.   **Adjustment to wind forcing**

A reduced-gravity model.   The simplest model to understand how the tropical oceans respond to an applied wind stress and how they reach a state of dynamic equilibrium (the spin-up problem) is the linear reduced-gravity (or 1.5-layer) model. This model has two immiscible layers of constant density ρ_1 and ρ_2, separated by an interface that represents the sharp and shallow tropical thermocline. The upper layer has a mean depth H_1 and is bounded by a rigid lid; the lower layer is infinitely deep and at rest. For simplicity, we only consider a spatially uniform zonal windstress τ^x (per unit specific volume), which acts as a body force in the upper layer; there is no stress at the interface. If η is the vertical displacement (positive upwards) of the interface, the shallow-water equations are

$$u_t - fv + g'\eta_x = \tau^x/H_1 \tag{61}$$

$$v_t + fu + g'\eta_y = 0 \tag{62}$$

$$g'\eta_t + c^2(u_x + v_y) = 0 \tag{63}$$

where $g' = (\rho_2 - \rho_1)g/\rho_1$ is the reduced gravity and $c = (g'H_1)^{1/2}$ the gravity wave speed. These equations are similar to (2.23)-(2.25), except that the pressure gradient term has been expressed in term of η. This is done by integrating the hydrostatic equation (2.8) between level z in layer 1 and level z* in layer 2, which yields

$$p(z) - p\ (z^*) = -\left[\rho_2(-H_1 - \eta - z^*) + \rho_1(z + H_1 + \eta)\right]$$

Taking the horizontal gradient then leads to $p_\alpha = \eta_\alpha(\rho_2 - \rho_1)$ since $p_\alpha(z^*) = 0$ as layer 2 is at rest. The pressure gradient can be thus expressed as a function of η as above. The following results can also be used to describe the adjustment of a continuously stratified ocean, using the normal mode representation.

As in (26), the equations can be combined into an equation for v

$$(v_{xx} + v_{yy})_t + \beta v_x - (v_{tt} + f^2 v)_t/c^2 = f\tau^x_t/c^2 H_1 \tag{64}$$

Since the forcing is *x*-independent (zonally uniform stress), the motion induced by a sudden onset of the wind at $t = 0$ is independent of longitude as long as the effects of the boundaries are not felt.

The equatorial jet. Before boundary effects are felt, Eq. (64) reduces to

$$v_{tt} + f^2 v - c^2 v_{yy} = -f\tau^x/H_1 \tag{65}$$

At large distances from the equator (i.e., at distances larger than the equatorial radius of deformation *L*), the third term is much smaller than the second, so that after a time much larger than the local inertial period, Eq. (60) reduces to

$$v = - \tau^x/fH_1 \tag{66}$$

which is the classical expression for the Ekman drift. For an eastward wind stress, the zonal currents vanish and the meridional currents are steady, converging on the equator in a way that amplifies as the latitude decreases. This convergence therefore induces a downwelling that intensifies toward the equator.

At the equator, however, the Coriolis term vanishes, so that the zonal momentum balance must be

$$u_t = \tau^x/H_1 \qquad \text{at } y = 0 \tag{67}$$

which implies that there is an accelerating zonal jet, and, from (62), a corresponding steady deepening of the thermocline.

To describe the transition between the equatorial and the mid-latitude regimes, consider times much longer than $T = (\beta c)^{1/2}$, so that the first term in (65) can be neglected, which filters the inertia-gravity waves that are excited by the onset of the wind. The solution is then

$$v = - \tau^x(\beta c)^{-1/2}Q/H_1 \tag{68}$$

$$u = \tau^x(1 - y*Q)t/H_1 \tag{69}$$

$$\eta = - \tau^x Q_{y*}t/c \tag{70}$$

where the function *Q* and the latitudinal structure of *u* and η are represented in Fig.3.4 de Philander (1990) as a function of the nondimensional meridional scale *y**. The solution represents an accelerating zonal jet whose half-width is twice the radius of deformation and which is always in geostrophic balance, a steady meridional current that asymptotes to the Ekman drift for large values of *y**, and a steady deepening of the thermocline near the equator. This solution is often refered to as the Yoshida jet. In case of easterlies, the accelerating equatorial jet is westward and there is steady upwelling. Note also that if the forcing stops, *v* tends to zero and the zonal jet becomes constant. In the absence of dissipation and boundary effects, the equatorial jet would persist indefinitely. This shows that the equatorial ocean has a memory, and that it integrates the forcing in more variable conditions.

In the presence of friction, a steady solution will be reached. In the simple case of equal Rayleigh and newtonian friction r, the steady solution is given by (68)-(70) with *1/r* instead of *t*.
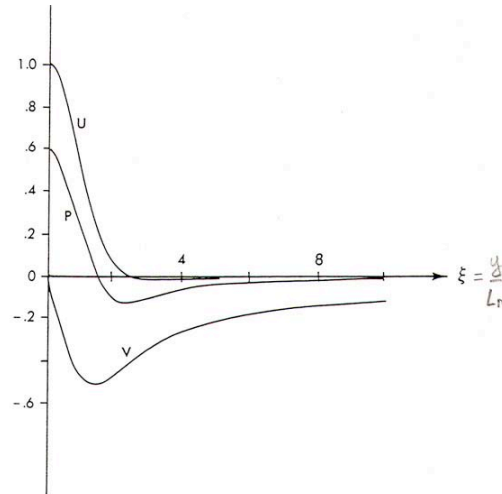
Figure 3.4. The latitudinal structure of the accelerating equatorial jet (U), of the steady meridional flow (V), and of the thermocline displacement (P) in response to spatially uniform eastward winds. The unit for latitude is the equatorial radius of deformation. [From Moore and Philander (1977).]

Equatorial adjustment. The Yoshida jet does not satisfy the boundary conditions at the meridional boundaries, so that the solution is only valid until the effects of the coasts are felt and an equilibrium state is reached. The adjustment to the final equilibrium is effected by equatorial waves generated at the boundaries. If the onset of the wind is gradual, the inertia-gravity waves play little role and the adjustment is due to Kelvin and Rossby waves. The zonal current response to the steady forcing can thus be written

$$u = u^{jet} + u^K + u^R \tag{71}$$

where the superscript jet, K and R refer to the Yoshida jet, Kelvin waves and Rossby waves, respectively. The boundary conditions at the meridional coasts are

$$u = 0 \quad at \; x = 0 \text{ and } x = x_E \tag{72}$$

At $t = 0$, Kelvin and Rossby waves are generated at the boundaries and propagate toward the interior of the basin. The Kelvin waves are the fastest, so we first consider the western boundary. To satisfy (72), eastward propagating Kelvin waves and short Rossby waves are available. However, only the Kelvin wave can transport mass zonally, as the short, slow Rossby waves only redistribute mass meridionally, but not zonally at low frequencies. The condition that the Kelvin wave returns the zonal mass flux associated with the jet

$$\int_{-\infty}^{\infty} u^{jet} dy = -\int_{-\infty}^{\infty} u^K dy \qquad at \; x = 0 \tag{73}$$

determines the Kelvin wave amplitude. Using (52), one finds

$$u^K = 0 \qquad\qquad\qquad\qquad for \; t < x/c$$
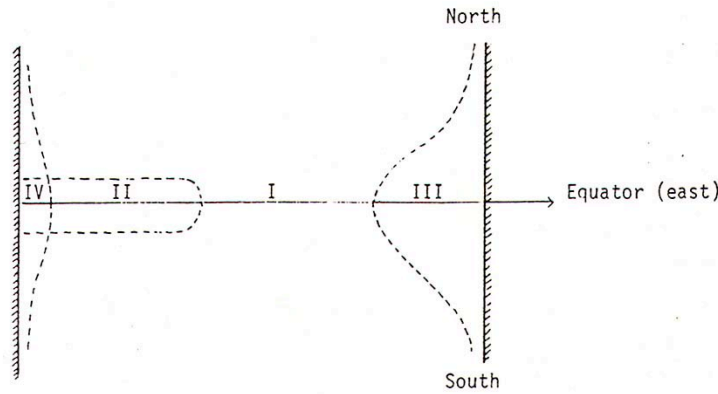$$= \alpha\tau^x(x - ct)/cH_1 \, exp(-y^2\beta/2c) \qquad\qquad for \; t > x/c \tag{74}$$

Figure 3.17. Schematic diagram that shows the distinct regions that characterize the oceanic adjustment to a sudden change in the winds.

where α is a constant equal to 0.84 (Cane and Sarachick JMR 1977). A front is thus excited at the western boundary at $t = 0$, and it travels eastward at the Kelvin wave speed c. After the front has passed, the acceleration of the jet is strongly reduced. At $y = 0$, the solution becomes

$$u = u^{jet} + u^K = (1 - \alpha)t\tau^x/H_1 + \alpha x\tau^x/cH_1 \qquad \text{for } t > x/c \qquad (75)$$

which shows that acceleration is reduced by a factor six. This happens because the front introduces a steady zonal pressure gradient in its wake, which nearly balances the wind stress at the equator. Indeed, from $u^K_t = - g'\eta^K_x$ and (69)-(70), one has

$$g'\eta^K_x = \alpha\tau^x/H_1 \, exp(- y^2\beta/2c) \qquad (76)$$

so that $g'\eta^K_x \approx \tau^x/H_1$ at $y = 0$. After the front, the horizontal motion becomes nearly nondivergent, and the meridional Ekman drift needs no longer be balanced by downwelling or upwelling.

The eastern boundary can be treated similarly, except that non-dispersive long Rossby waves are excited and propagate westward. Because the jet is symmetric about the equator, only the odd Rossby modes are excited. The fastest mode is the $m = 1$ mode which travels at speed $c/3$ and has the narrowest width, then the $m = 3$ mode which is less equatorially trapped, and so on. The Rossby wave fronts introduce a zonal pressure gradient, and in their wake the jet become practically steady (Fig.3.18 et 3.19 de Philander (1990)). After a time $3x_E/4c$, the Kelvin and Rossby fronts meet at the equator, and there is a zonal pressure gradient all along the equator. The Kelvin and Rossby wave fronts then propagate in regions already affected by the boundary effects and start to decelerate the equatorial jet. The Kelvin wave reaches the eastern boundary and is reflected westward, with some energy loss to the high latitudes, and the Rossby waves reach the western boundary and generate a Kelvin wave. The equatorial ocean is essentially adjusted when the reflected waves reach the opposite boundary, i.e. after time $4x_E/c$. The remaining oscillations

disappear rapidly, because of eastern boundary energy leakage toward the high latitudes and, at least in numerical simulations, dissipation.
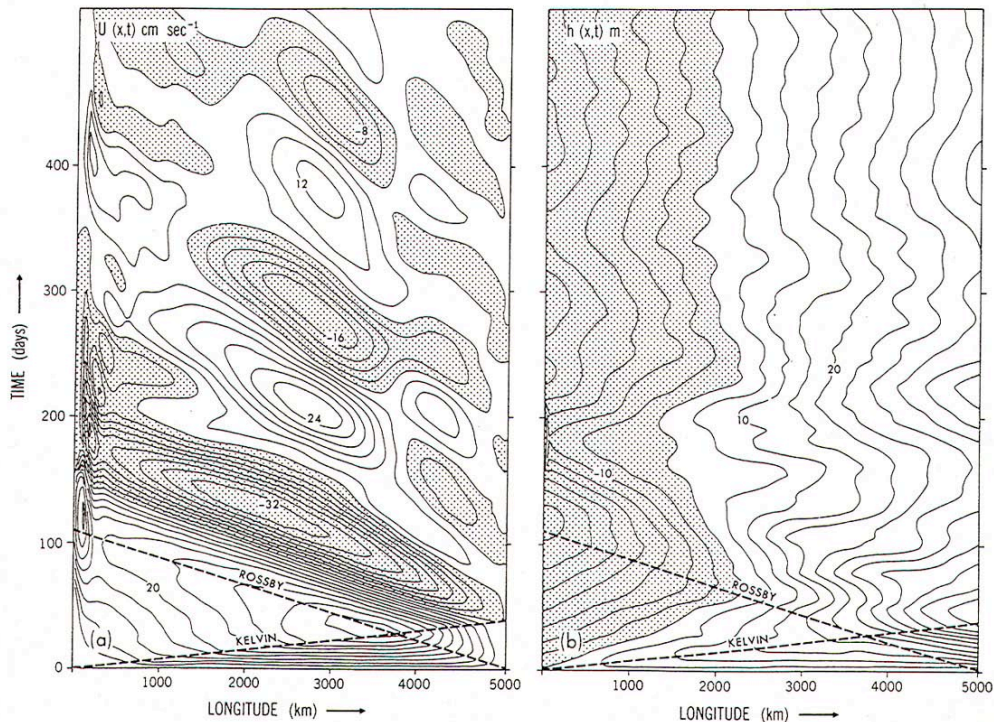

Figure 3.18. Changes in the zonal velocity component (centimeters per second) and in departures from the mean depth of the thermocline along the equator after the sudden onset of spatially uniform eastward winds. The dashed lines indicate the speeds at which Kelvin and the gravest Rossby mode propagate. The thermocline is elevated and motion is westward in shaded areas.
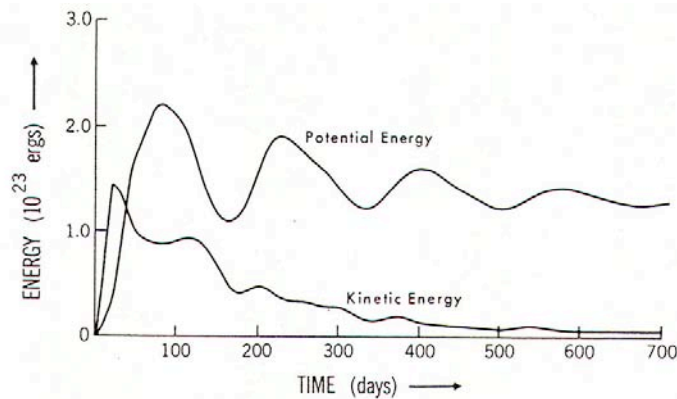
Figure 3.19. The kinetic and potential energy for the latitude band 5°N to 5°S for the motion in Fig. 3.18.

The adjustment time of the equatorial ocean depends on is width, and, in more realistic cases, on the importance of the various vertical modes. Model results suggest the adjustment of the upper equatorial ocean is primarily done by the second vertical mode, so typical values are 450 days for the equatorial Pacific, and 150 days for the equatorial Atlantic. The response to seasonal forcing can thus be in near equilibrium in the smaller Atlantic Ocean, but not in the

equatorial Pacific. The adjustment is slower away from the equator, as only Rossby waves are available for the adjustment, and they propagate more slowly as the latitude increases.

In the inviscid reduced-gravity model, the steady state is a motionless state where the wind stress is exactly balanced by a zonal pressure gradient

$$g'\eta_x = \tau^x/H_1 \tag{77}$$

The thermocline has a constant slope, deepening westward in case of easterlies, in qualitative agreement with the observations (Fig.6). The motionless state is not realistic, however, and the model is unable to simulate the presence of an undercurrent. This remains true if the nonlinearities are retained in the 1.5-layer model, which simply has a too rudimentary vertical structure to provide an adequate description of the currents in the equilibrium state. In this model, the upper layer is in uniform motion, and so uniformly "feels" the windstress. In reality, the turbulent surface layer feels the stress but the deeper fluid only feels the pressure force. Thus, a better vertical resolution is needed, and the vertical stress must be better modeled. In spite of these limitations, the reduced-gravity model is useful as it provides a good description of the transient part of the adjustment process. If the wind stress is not uniform but has a curl, the steady state solution away from the equator has an additional Sverdrup flow (see Philander 1990).

Cane (1979) has shown that a straightforward extension of the reduced-gravity model could already produce an equatorial undercurrent and reveal important dynamical features. The upper layer is divided into two layers of identical density, which can exchange mass and momentum. The wind stress is only felt in the surface layer, which has constant depth for simplicity, and there is an interfacial stress between the two layers, which is proportional to the shear. In the simplest model version, there is no stress at the interface with the deep layer, which remains at rest. In the linear case, it can be shown that the vertically averaged velocity over the top two layers obeys the same equations than in the reduced-gravity model, so that its equilibrium value in the presence of a uniform zonal wind stress is again equal to zero. However, there is a a steady state current in the direction of the stress in the surface layer, and in the opposite direction in the layer below, as the interfacial stress is too weak to balance the pressure gradient. Friction can thus produce some of the observed features of the equatorial undercurrent, but the model currents are too weak and there is no net zonal mass transport as in the observations. More realistic features are found in the nonlinear case, however, since the inertial term plays an important role in the undercurrent dynamics. Because of the importance of the nonlinearities, general circulation models (GCM) are needed to properly simulate the Equatorial Undercurrent, with a high vertical resolution in view of the complexity of the near surface mixing.
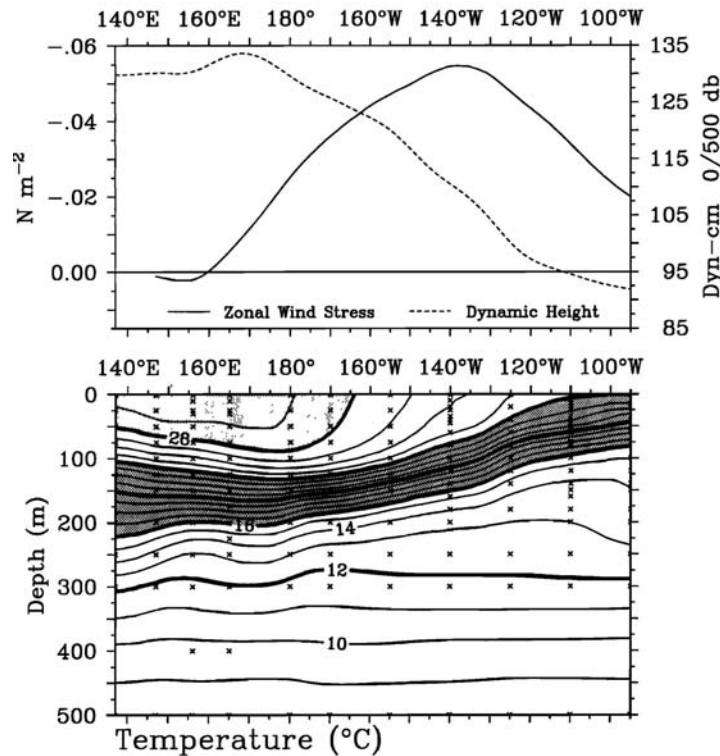
Figure 6. Zonal section of mean temperature averaged between 2°N and 2°S on the basis of available TAO time series data in 1980–1996. Also shown is the corresponding mean zonal wind stress (computed using a constant drag coefficient of 1.2×10^{-3}) and dynamic height 0–500 dbar (computed using mean temperature/salinity relationships based on work by *Levitus and Boyer* [1994] and *Levitus et al.* [1994a]). Crosses indicate depths and longitudes where temperature data were available. An average at a particular location was computed only if a minimum of 2 years of data was available.

The behaviour of the equatorial ocean under time varying forcing is of interest to understand its role in the ENSO phenomenon. Neelin et al. (JGR 1998) has considered a 1½ layer model with a 250-day damping time forced by a zonal wind patch that is limited to the central Pacific and oscillates with a 3-year period, which corresponds to the dominant ENSO period. The steady state response to the forcing if it were steady is shown in Fig. 2. Note that the thermocline is flat at the equator outside the zone of wind forcing, consistent with (77), but that it is tilted away from the equator. The time evolution of the equatorial thermocline under periodic forcing is shown in Fig. 3. Since the 3-yr period is much longer than the equatorial adjustment time, the model is nearly in equilibrium at the equator. Away from it, however, there are large departures from equilibrium best seen in Fig. 5, where the equilibrium solution (pattern in Fig. 2 multiplied by the wind stress amplitude) has been subtracted. Note the off-equatorial westward propagation of the lines of equal phase, which corresponds to the propagation of the Rossby waves that are too slow to adjust to the changing wind, in particular far away from the equator where their westward propagation speed is slowest. Figure 5 illustrates the extra-equatorial "ocean memory" that plays a key role in the ENSO phenomenon and accounts for much of its predictability: the upper ocean heat content away from the equator is not in equilibrium with the wind, and it will later feed the equatorial zone and the eastern basin via the western boundary and Kelvin waves.
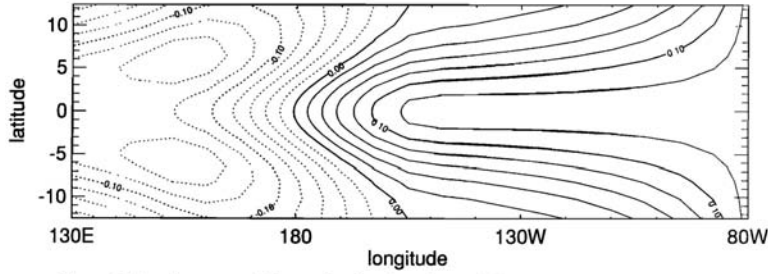
Figure 2. Steady response of thermocline depth in a linear shallow water model to steady wind forcing, constant in latitude. The longitude dependence is a half sinusoid centered on the date line and with half wavelength 60°, zero elsewhere.
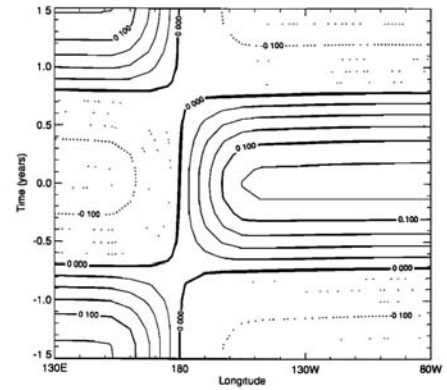

Figure 3. Time-longitude evolution of thermocline depth along the equator from a shallow water model forced by a 3-year period oscillating wind stress path centered at the date line. The calculation is akin to *Cane and Sarachik* [1981], except that the wind stress patch has more ENSO-like longitudinal dependence.
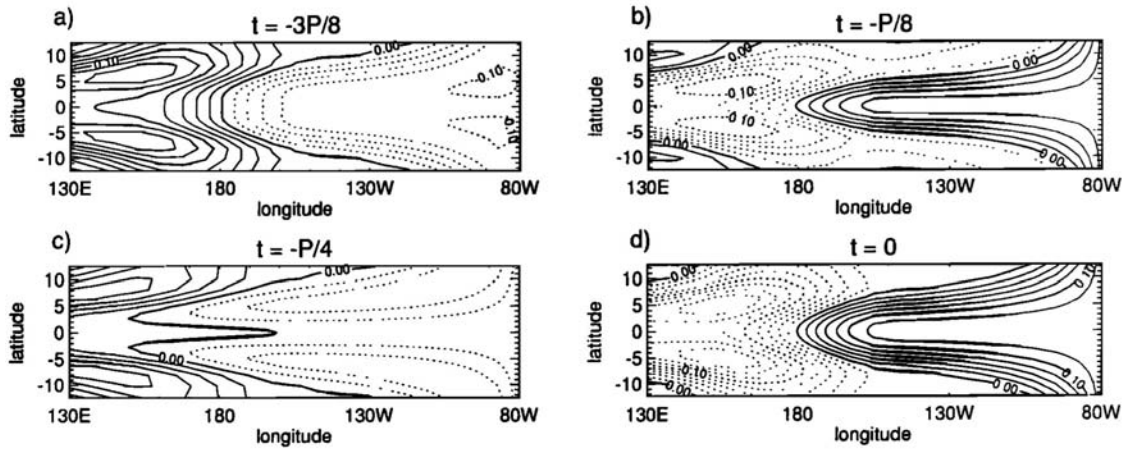
Figure 4. Latitude-longitude evolution of thermocline depth (also proportional to ocean surface height) from a shallow water model forced by the oscillating wind stress patch of period $P = 3$ years, as in Figure 3. Time is indicated in fractions of a period prior to the maximum westerly phase of the winds.
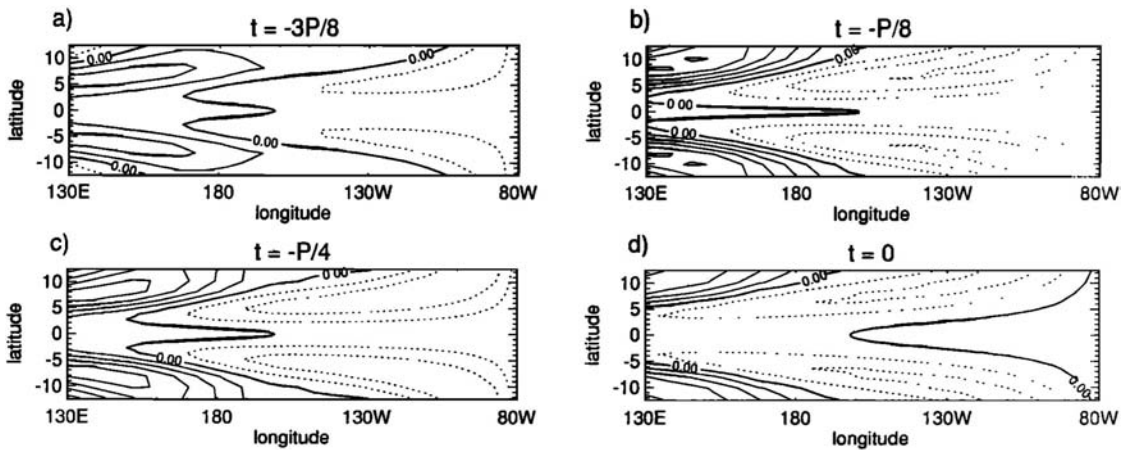

Figure 5. The "ocean memory" component of the thermocline depth response in Figure 4. Here ocean memory is defined as the difference between the actual solution and the part of the solution explained by instantaneous balance with the wind stress. This definition is useful at timescales long compared to the Kelvin crossing time, such as ENSO timescales, where steady balance explains much of the solution but where the departures from steady balance are crucial to further evolution.

The observed variability of sea level and thermocline depth is rather well reproduced by an ocean model forced by the observed wind. This is seen in the figure below (Busalacchi et al. JGR 1983) based on a 1.5 layer model, although a GCM forced by better winds would provide a more realistic simulation and, in particular, better currents. In any case, it demonstrates that the tropical ocean behavior is largely controled by the wind.
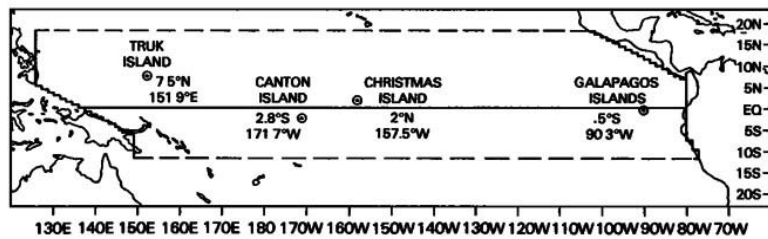

Fig. 1.   Comparison of the model geometry with the tropical Pacific Ocean. The model basin extends from 18°N to 12°S and from 126°E to 77°W. The dashed line represents an open boundary; all remaining boundaries are solid walls. Sea-level data from the island stations indicated provide details of the interannual variability in different regions of the Pacific.
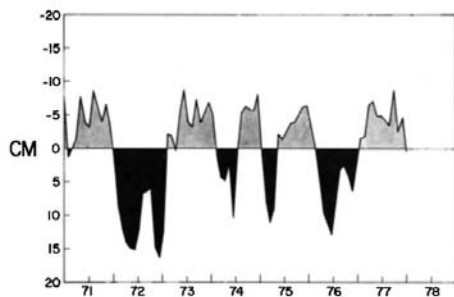

Fig. 2.   Time series of observed sea level at the Galapagos Islands from 1971–1977, inclusive. Data for 1978 are not available. Periods when the mean monthly sea level is higher than the long-term annual mean are shaded black.
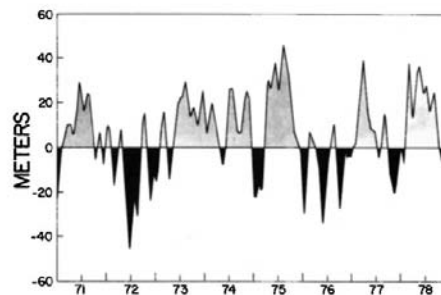
Fig. 3.   Model pycnocline height anomaly (PHA) at the Galapagos Islands. Periods when the pycnocline is deeper than the mean for 1961–1978 are shaded black.
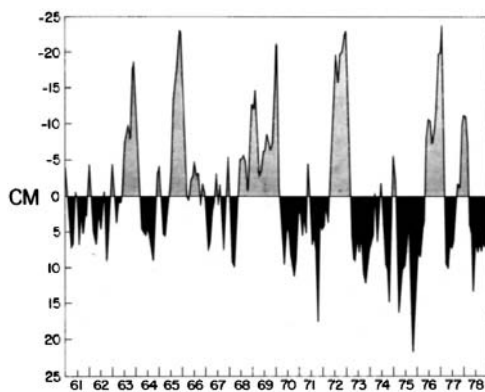
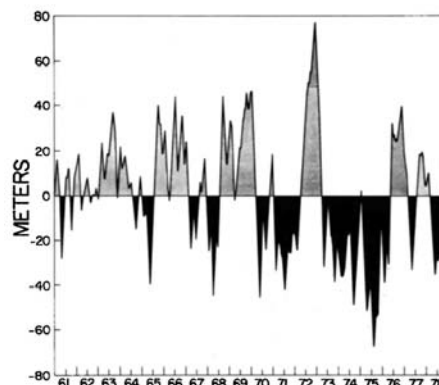Fig. 6.   Time series of observed sea level at Truk Island from 1961–1978, inclusive.

Fig. 7.   Model pycnocline height anomaly for 1961–1978 at a location corresponding to Truk Island.

3. Instability waves

The observations show that the equatorial currents become unstable during certain seasons, when the horizontal shear become very large. This happens when the

trade wind intensify, equatorial upwelling increases, and the SST along the equator decreases. As the SST north of the equator does not change substantially, a SST front appears mear 3°N and the meridional shear between the South Equatorial current and the North Equatorial Countercurrent mean current increases, resulting in instabilities near 3°N, which are illustrated below for the tropical Atlantic, where they appear in May and are seen for a few months. In the Pacific, they are seen in longer periods (Philander 1990). These instabilities propagate westward with a period of 20 – 30 days and a wavelength of teh order of 1000 km. The waves have a large amplitude, with a meridional velocity reaching 80 cm/s and a large vertical excursions. They are trapped in the surface layer and contribute significantly to diffusing the mean
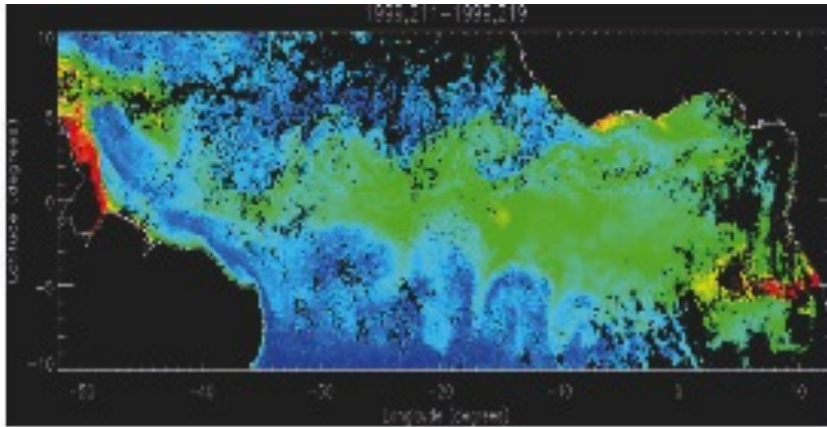

Fig. 1. TIWS as seen by SeaWiFS (courtesy of M. Ux). Note the cusps in ocean color along 4°S and 4°N.

mean momentum and transporting heat equatorward, thus warming the equatorial waters (Bryden et Brady, JMR 1989). The waves are due to the instability of the shear currents. This can be modelled simply by adding a zonal mean flow *U(y)* in geostrophic balance to the reduced-gravity model (Philander, JGR 1978, Fig. 1). The mean thermocline depth *H(y)* is then given by

$$fU + g'H_y = 0 \tag{78}$$

After linearization, the equations for a perturbation become

$$u_t + Uu_x + U_y v - fv + g'\eta_x = 0$$

$$v_t + Uv_x + fu + g'\eta_y = 0 \tag{79}$$

$$\eta_t + U\eta_x + (Hu)_x + (Hv)_y = 0$$

Assuming that the time and zonal dependance of the perturbations is in *exp(ikx – ωt)*, one finds that, for given *k*, the complex frequency *ω* is the eigenvalue of a second-order differential
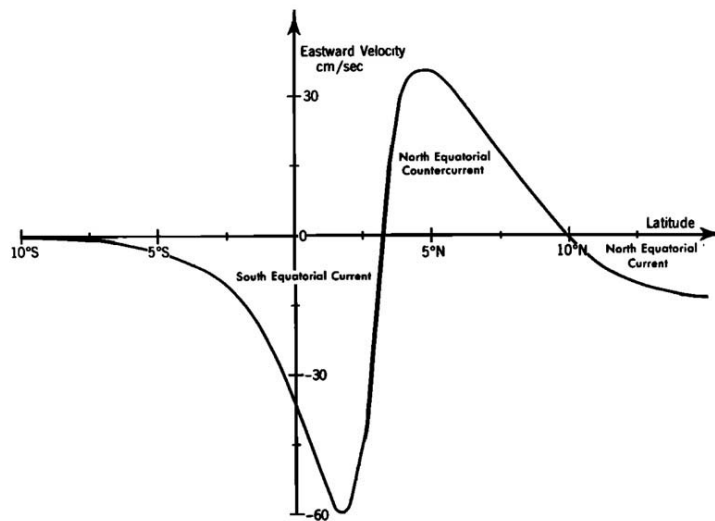
Fig. 1. Latitudinal variation of the mean zonal flow in the surface layers of the ocean.

equation in y. For a realistic profile, the equation must be solved numerically. The perturbations grow when the shear is large enough, with maximum growth as observed for wavelength of about 1000 km and period of about 30 days. This is illustrated below for different amplitudes of the zonal currents, taken as the maximum speed of the SEC (from Philander 1990).
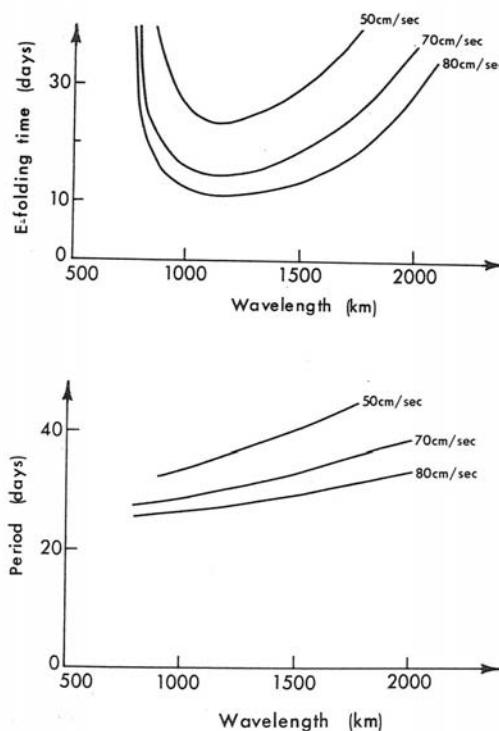

Figure 3.23. The *e*-folding time and period as a function of wavelength of waves associated with instabilities of the surface currents shown in Fig. 2.1. The curves correspond to different amplitudes of the zonal current. The shape of the profile $U(y)$ is the same for all the calculations, but the amplitude, which is taken to be the maximum speed of the South Equatorial Current, is varied. [From Philander (1978b).]